Topographic measurement of buried thin-film interfaces using a grazing resonant soft x-ray scattering technique

Eliot Gann, Anne Watson, John R. Tumbleston, Justin Cochran, Hongping Yan, Cheng Wang, Jaewook Seok, Michael Chabinyc, and Harald Ade

Phys. Rev. B **90**, 245421 — Published 15 December 2014

DOI: 10.1103/PhysRevB.90.245421

Topographic Measurement of Buried Thin-Film Interfaces Using a Grazing Resonant Soft X-Ray Scattering Technique

Revised 11/19/2014

Eliot Gann[1*], Anne Watson[1], John R. Tumbleston[1], Justin Cochran[2], Hongping Yan[1], Cheng Wang[3], Jaewook Seok[4], Michael Chabinyc[2], Harald Ade[1*]

[1] *Department of Physics, NCSU, Raleigh, NC 27695-8202.*
[2] *Materials Department University of California, Santa Barbara, CA 93106-5050.*
[3] *Advanced Light Source, LBNL, Berkeley, CA 94795.*
[4] *Department of Materials Science and Engineering, NCSU, Raleigh, NC 27695-8202.*
[*] ***Corresponding Authors**: ehgann@ncsu.edu (E.G.), harald_ade@ncsu.edu (H.A.)*

The internal structures of thin films, particularly interfaces between different materials, are critical to system properties and performance across many disciplines, but characterization of buried interface topography is often unfeasible. In this work, we demonstrate that Grazing Resonant Soft X-ray Scattering (GRSoXS), a technique using diffusely scattered soft X-rays in grazing incidence geometry, can reveal the statistical topography of buried thin film interfaces. By controlling and predicting the X-ray electric field intensity throughout the depth of the film and simultaneously the scattering contrast between materials, we are able to unambiguously identify the microstructure at different interfaces of a model polymer bilayer system. We additionally demonstrate the use of GRSoXS to selectively measure the topography of the surface and buried polymer-polymer interface in an organic thin film transistor, revealing different microstructure and markedly differing evolution upon annealing. In such systems, where only indirect control of interface topography is possible, accurate measurement of the structure of interfaces for feedback is critically important. While we demonstrate the method here using organic materials, we also show that the technique is readily extendable to any thin film system with elemental or chemical contrasts exploitable at absorption edges.

Keywords: Interface Structure, Thin Film Morphology, Organic Electronics, X-ray Scattering, Organic Thin Film Transistors, Soft X-ray Scattering, Resonant Scattering, Grazing Incidence Scattering, RSoXS, GRSoXS, GISAXS, Synchrotron Techniques

PACS: 68.35.bm, 81.05.Fb, 83.85.Hf

I. INTRODUCTION

The properties and performance of thin films often stem from the physical morphology, particularly roughness and interdiffusion at interfaces between their component materials. [1-3] By their very nature, scanning probe methods can only characterize exposed surfaces. [4] Microscopies of buried interfaces can be powerful, but are inherently local and require preparation of cross sectional samples using methods that may damage the interface particularly in the case of soft materials. [3, 5] For any measurement using radiation or particles that penetrate into thin film samples to probe buried structure, such as grazing incidence X-ray or neutron scattering, the excess signals generated from the bulk along this path often dwarf the specific signal of interest. If the signal of interest can be varied relative to the background to create contrast, such techniques can allow quite accurate measurement of the particular features of interest, but unfortunately in many cases control over particular material contrast or depth sensitivity is not possible. Grazing Resonant Soft X-ray Scattering (GRSoXS) is a novel technique that uses two parameters simultaneously to accomplish this signal variation: angle of incidence variation and selection of soft x-ray spectroscopic resonances specific to particular chemical structures.

Specular X-ray or neutron reflectivity methods lack sensitivity to in-plane structure [6-8] (Fig. 1A) and so, while they are quite useful in measuring thicknesses and RMS (root mean squared, out of plane) roughness, they cannot easily determine the texture of that roughness. Complementary alternatives are diffuse, off-specular X-ray or neutron scattering techniques. [9-14] Grazing incidence X-ray scattering using the distorted wave born approximation (DWBA), can exploit an incident angle dependent X-ray Electric Field Intensity (XEFI) distribution to enhance or suppress scattering from certain depths within a thin film. Conventional X-ray methods (Fig. 1B) however, rely on electron density differences for contrast, [9, 15] which often provide both insufficient and unchangeable contrast in

systems composed of similar populations of low Z elements, [9, 16] leaving features such as a particular internal interface between materials impossible to probe. Neutron scattering can generate additional contrast at interfaces (Fig. 1C) but this contrast is not tunable *in situ* and often requires preparation of multiple samples with different isotopic substitutions, [9, 10, 17] so the problem of picking out the unique signal from just the interface is not straightforward. Despite the limited penetration depth compared to neutron based techniques (Neutrons have a penetration depth through carbon of several centimeters, while soft X-rays, even below the C Kα absorption edge have a penetration depth of about 1 micron), resonant X-ray methods have demonstrated large, selective and continuously variable contrast where X-rays of different energies have been shown to selectively probe specific pairs of materials. [18, 19] However, current resonant scattering methods, exploiting an absorption edge to reveal the structure between specific materials, have either not used grazing incidence, or if so, have not utilized the DWBA to reveal internal interface structure below the surface, rather only using surface sensitivity at absorption peaks [20, 21] or only studying bulk properties. [22, 23]

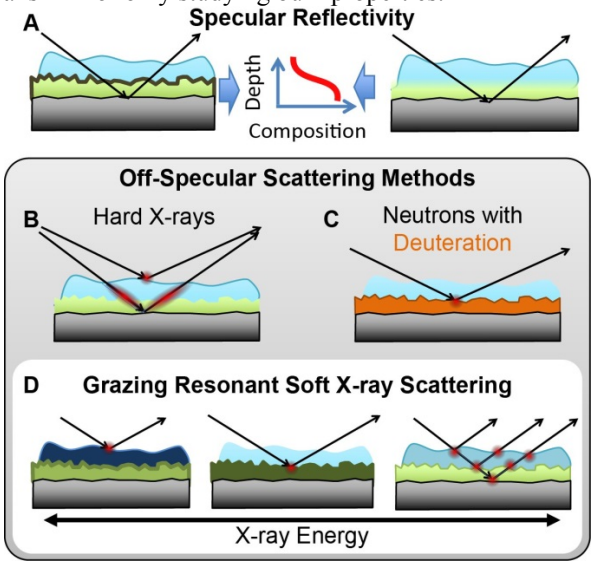

Figure 1 Methods to measure buried interfaces.
An illustration showing the difficulty of measuring a buried internal interface in a bilayer by established techniques. Red highlighted areas illustrate the locations of sensitivity. A) X-ray and neutron reflectivity only reveal composition gradients normal to the interface and are insensitive to in-plane correlation lengths. B) Many grazing-incidence probes can isolate the surface and probe the bulk, but cannot readily distinguish individual layers. C) Neutrons probe with a single fixed contrast for a given sample, but through methods such as deuteration, sensitivity to the interface can be greatly increased. D) Using GRSoXS, on a single sample, each of the signals from different sites can be controlled by choice of X-ray energy.

The technique presented in this work, GRSoXS, successfully combines tunable contrast of resonant soft X-rays, [24-26] and use of DWBA and control of the XEFI that occurs at grazing angles [14, 27] to gain specific sensitivity to internal interfaces many nanometers below an exposed surface (Fig 1D). As exploited previously, the DWBA predicts how the XEFI of a probe X-ray beam is produced in the sample as the reflected and transmitted electric fields interfere and photons are absorbed and scattered. On the other hand particular material pairs can be distinguished by contrast control resulting from differences in the molecular bonding environment of constituent materials. This chemical contrast and the XEFI both strongly, and in very different ways, depend on the complex index of refraction n at depth z in the film shown in Fig. 2A for two polymers near the carbon absorption edge. The relative simulated scattered intensity (A_{sim}) from a given site in a film is the product of the probability of an X-ray scattering to a particular direction from the materials at a site (determined from the contrast calculation and morphology present) and the probability of an X-ray being at that site (determined from the DWBA). To first order these are respectively represented by the materials contrast $\left|\Delta n(z)\right|^2$ at the corresponding depth (z) (Fig. 2B for the two materials in the model system discussed in the next section) and the XEFI at that incident angle (θ) and X-ray energy (E) and depth (shown in Fig.3A).

$$A_{\text{sim}}(E,\theta,z) \equiv \left|\Delta n(z)\right|^2 * XEFI(E,\theta,z) \qquad (1)$$

In this simplified theory, the scattered beam has no further interactions with the system, apart from refraction upon leaving the film. In some systems, the optical path on the way out may result in internal reflection from the top interface, or absorption in the top layer, which are not accounted for in this theory. Absorptive effects of the scattered wave are generally significantly less than that of the incident waves, which are at or near the critical angle and so suffer maximally from absorption effects. In addition, because we deal with planar systems, refractive effects will largely affect the out of plane scattered angle, which is inconsequential since we integrate over these angles in the analysis to find in-plane structure. In this theory, calculating in-plane scattering intensity requires a model consisting of the constituent materials, layer thicknesses and approximate out-of-plane roughnesses in the system. This model is created with knowledge of how the film was created, but can be refined iteratively to match the measured intensities or determined independently by reflectivity. Specular reflectivity is a natural complement to GRSoXS because *n(z)* can be precisely determined through fitting of a reflectivity profile, which in turn can be used as input for the DWBA model.

We use Parratt's multilayer solution with a slicing algorithm to simulate the XEFI throughout a device. Using

the material concentration depth profile through a device, an average index of refraction at every 1 Å thick layer is determined. At every layer we calculate the Fresnel reflectivity r_{ij} and transmission t_{ij},

$$r_{i,j} = \frac{k_{z,i} - k_{z,j}}{k_{z,i} + k_{z,j}} \quad (2)$$

$$t_{i,j} = \frac{2k_{z,i}}{k_{z,i} + k_{z,j}} \quad (3)$$

For each interface $j = i \pm 1$ by allowing the transverse electric field component to remain constant (for s polarization of the incident X-rays) we use the following recursive relationships between the electric field components in each layer.

$$E_{\uparrow i} = \frac{e^{ik_i d_i}}{t_{i,i+1}} \frac{1}{r_{(i,i+1)} E_{\downarrow i+1} + E_{\uparrow i+1}}, \quad (4)$$

$$E_{\downarrow i} = \frac{e^{-ik_i d_i}}{t_{i,i+1}} \frac{1}{E_{\downarrow i+1} + r_{(i,i+1)} E_{\uparrow i+1}} \quad (5)$$

Setting the boundary conditions to normalize for the incident beam $E\downarrow(0) = 1$, and setting no electric field travelling up from within the substrate itself $E\uparrow(n) = 0$, the electric field of both the incoming (direct) and outgoing (reflected) electric field components can be recursively solved within every layer. With small changes in angle, the r and t can change drastically, while at different X-ray energies the effective index of refraction changes. These effects combine to make XEFI vary in a complex three dimensional parameter space. An example of the complexity of this three dimensional parameter space is shown in Fig. 3A with isosurfaces representing different levels of XEFI penetration into the model system discussed in the next section.

The slicing algorithm allows simulation of arbitrary RMS (out of plane) roughnesses, although in-plane coherence lengths at each layer (ξ) are not taken into account. Corrections are available to the Parratt formalism [27] which take the distribution of coherence lengths at each interface and the correct ξ parameters to be used in this correction are exactly those measured by GRSoXS. Thus, GRSoXS experimental results can be fed back into the simulation to more accurately predict the XEFI, however for the experiments in this work, agreement with initial simulations was very good, and this level of iteration was not required.

In the X-ray regime, the refractive index of organic materials is very close to 1, so that we split out the real (δ) and imaginary (β) parts of the deviation from 1 in a conventional approach as:

$$n(E) = 1 - \delta(E) + i\beta(E) \quad (6)$$

Whereas with hard X-rays we would relate this to the electron density (ρ) within a material, and define the contrast to be proportional to $\Delta\rho^2$, with X-rays near an absorption edge we instead leave it in terms of Δn^2. Thus to calculate the contrast of a feature composed of two elements with refractive indices n_1 and n_2 is $(n_1 - n_2)^2$, which is given by (3) derived from (2):

$$|\Delta n|^2 = (\delta_1 - \delta_2)^2 + (\beta_1 - \beta_2)^2 \quad (7)$$

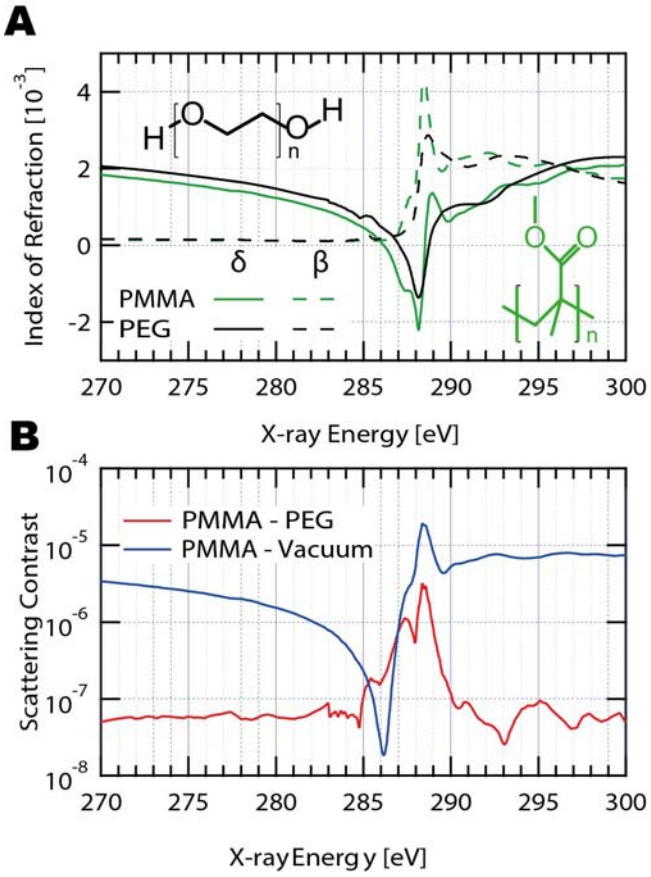

Figure 2 Optical Constants and Contrast for Experiment 1 A) Real deviation from 1 and imaginary components of the index of refraction for PMMA and PEG. Inset are molecular structures of (left) PEG and (right) PMMA B) Contrast for the top surface and interface.

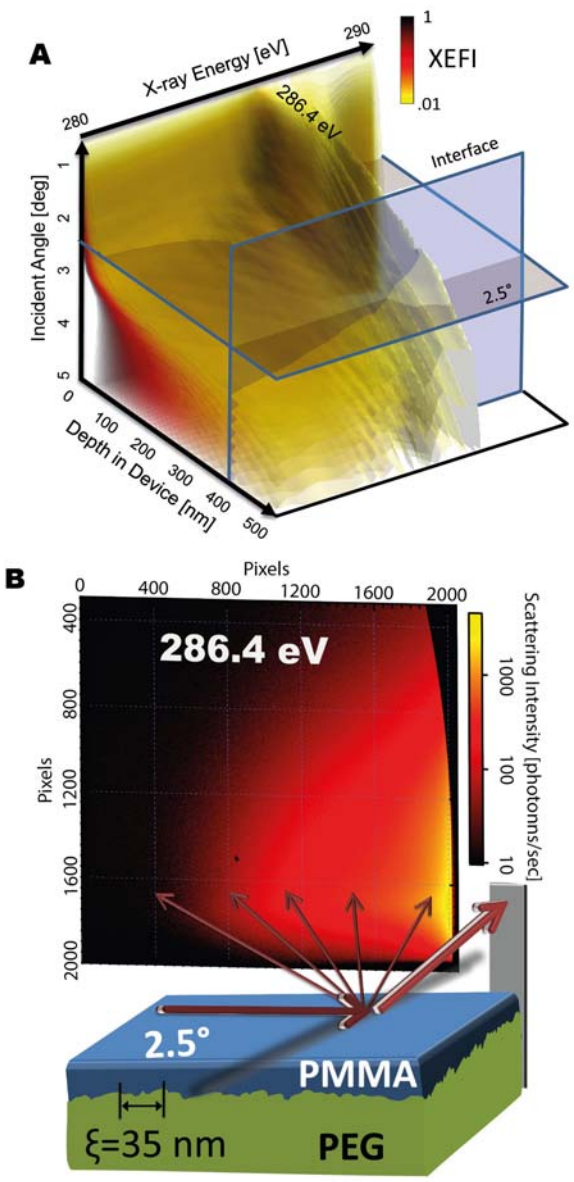

Figure 3 Experiment 1 XEFI calculation and Schematic A) A 3D semitransparent isosurface plot of calculated XEFI vs. energy, incident angle and depth for the PMMA PEG system. Isosurface values are 1% (yellow) – 100% (black) of the incident intensity. The slices of this space corresponding to the interface (at a depth of 400 nm) and 2.5 degrees incident angle are outlined.[28] B) Schematic of acquisition geometry with example raw scattering pattern and the PMMA PEG sample. The directly reflected X-rays are stopped by the beamstop, while the off specular scattering is captured in the 2D detector.

II. EXPERIMENT 1 MODEL BILAYER

By examining a bilayer system, the situation is simplified in two important ways. First, all interfaces are parallel to the substrate, which means determining interfacial structure will only require examining the in-plane component of scattering. Therefore, as discussed above, refraction of the scattered beam will be in the vertical direction, which, because we integrate vertically to create an in-plane scattering profile, does not matter to our calculation. It also means that collecting a large range of scattering angles requires detector movement in only one dimension.

The second benefit of considering bilayer systems is that the sources of scatter become somewhat straightforward to determine. There is potential scattering from the top surface, the buried interface, the substrate interface (if there is a substrate), and bulk scattering within the top layer, bottom layer, and substrate. We can eliminate the bulk scattering by having homogenous materials (they need only be homogeneous at the size scales we are collecting scattering, so 10s of nm and higher). Additionally, by making the lower layer effectively infinitely thick, we can eliminate the substrate effects. In this we can create an ideal binary scattering system, where the only significant sources of scatter are the top surface and buried interface.

To check that equation (1) is a viable model and to verify the potential linear independence of scattering signals from a top surface and buried interface in a well characterized sample, a bilayer of two chemically distinct polymers was engineered to have a buried interface with a designed dominant in-plane correlation length $\xi \cong 35$ nm, which would be straightforward to pick out in a potentially complex scattering pattern. A thick substrate of poly(ethylene glycol) (PEG) was molded with this structure and crosslinked to be resistant to temperature changes and solvents (described in methods section). A top layer of ~400 nm of poly(methyl methacrylate) (PMMA) was applied to the PEG and held above melting temperature for several hours to ensure the top PMMA-vacuum surface had a low RMS roughness and a much larger ξ than the molded, buried interface. The two amorphous polymers of this system were chosen to yield low bulk scattering and for ease of sample creation, not for high scattering contrast. Indeed, the spectra of the two materials are relatively similar (Fig. 2A), and the material contrast (Fig. 2B) is correspondingly small. The overall schematic of the experimental and sample geometry is shown in Fig. 3B. Because these two materials are carbon based, we utilize the rich spectroscopic variances available at the Carbon Kα absorption edge between 280 eV and 290 eV for these experiments.

Figure 4A shows in-plane diffusely scattered 281.6 eV X-rays collected from this engineered sample. By integrating over the out-of-plane dimension (between the dashed yellow lines) and applying a Lorentz correction[16] we produce the scattering intensity $I_1(q)$, representing a distribution of in-plane spatial frequencies from within the sample, shown in Fig. 4B.

An empirical fit of the scattering distribution uses constituent Gaussians corresponding to a physical ξ that only change in amplitude $A_{\mathrm{exp}}(E,\xi)$ with energy. The success of the fit in capturing the scattering features and reducing them to a manageable parameter space is evident by comparison of the data and fit vs. energy in the lower panels of Fig. 4B. The empirical fit captures the two size-scale distributions that are readily seen in 2D data, which are clearly associated with specific energy ranges. The fact that there are exactly two clear distributions already indicates a connection to the two designed sites of scatter in this sample: the surface and the interface.

To identify the corresponding scattering sites, $A_{\mathrm{exp}}(E,\xi)$ of the most prominent ξs from the fit (37 nm and 680 nm) are plotted vs. energy in Fig. 4C along with the simulated $A_{\mathrm{sim}}(E,z)$ from the surface and interface. Comparison of the experimental and simulated scattering intensities definitively identifies the dominant correlation lengths at the surface and interface as ξ_{surf} =680 nm and ξ_{int} =35 nm respectively. The scatter corresponding to ξ=160 nm was found to have a similar energy dependence, but lower intensity than that at 680 nm, and so must also be a surface feature. Although, in this case there are only two apparent sites of scatter, which makes the identification of each trivial, we can further explore the signal to background variation by defining an interface sensitivity $S(E)$ of the measurement and simulation, as the percentage difference between respective intensities at the buried interface and top surface (Fig. 4D).

$$S_{sim}(E) \equiv \frac{\gamma A_{sim}(E,z_{int}) - A_{sim}(E,z_{surf})}{\gamma A_{sim}(E,z_{int}) + A_{sim}(E,z_{surf})} \qquad (8)$$

$$S_{exp}(E) \equiv \frac{A_{exp}(E,\xi_{int}) - A_{exp}(E,\xi_{surf})}{A_{exp}(E,\xi_{int}) + A_{exp}(E,\xi_{surf})} \qquad (9)$$

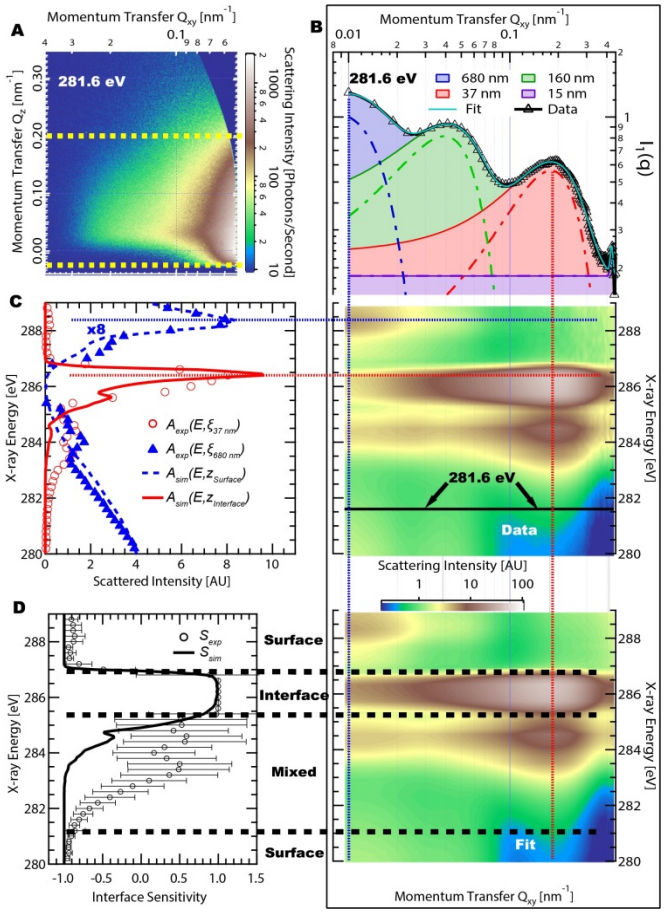

Figure 4 Identifying Scattering Elements.
A) A normalized and background corrected exposure acquired at 281.6 eV at the high q_{xy} detector location. The dotted yellow lines correspond to the limits of vertical integration which result in B) Scattering intensity and fit as function of momentum transfer. (Top panel) Scattering intensity at 281.6 eV and fit with Gaussian components corresponding to four dominant ξs. (Middle panel) measured scattering intensity at all energies and (Bottom panel) resulting fit. C) Intensity fit at 680 eV and 37 eV with scaled Simulated scattering intensity from the surface and interface. D) Measured and simulated interface sensitivity. Error bars are calculated from normalization uncertainty.[29] C and D are displayed with energy on the vertical axis for direct comparison with the data in B. Dotted red and blue lines are guides to the eye where the interface and surface scattering are highest in energy and momentum transfer. Dashed black lines across the bottom of the figure separate energy regions where the surface or interface sensitivity dominates.

To provide an informed comparison of the energy dependence between experiment and simulation, a scaling factor γ is found by scaling A_{sim} to the corresponding

A_{exp} as in Fig. 4C. While the energy and angular dependence of scattering intensities can be simulated accurately, the independent scale factor γ between scattering from the interface and surface varies depending on the specific microstructure, and so is in this case set experimentally to graphically compare the energy dependence of the experiment to the simulation. This factor can be understood to reduce linearly with the RMS roughness of a surface. Even if the materials have high contrast and X-rays reach the interface (the XEFI is high), if there are no in-plane scattering features to scatter from, no X-rays can be scattered in an off-specular direction. Similarly if the roughness is at a size scale which is not captured experimentally, the experimental scattering intensity must be scaled accordingly.

While experimental uncertainty in regions of mixed sensitivity seems to be high, it is only the parameters at which the interface or surface can be individually probed with high fidelity that are of immediate interest, where $S \approx \pm 100\%$ respectively. The full scattering patterns collected with these index-matched parameters can reveal further details of the topography present beyond the simple Gaussian fit we employed to find them, and is explored further below.

III. EXPERIMENT 2 OTFT BILAYER

To demonstrate the value of GRSoXS to electronic devices, a model bilayer relevant to organic thin film transistors (OTFTs) with poly(styrene) (PS), a gate dielectric, on top of poly(2,5-bis(3-tetradecylthiophen-2-yl)thieno [3,2-b]thiophene) (PBTTT), a semiconductor, was characterized by following the methodology delineated above.[30] Charge transport in OTFTs occurs solely at the interface between the semiconductor and the dielectric [31, 32] and the interface topography is known to be critical to device performance, but until now has not been measured directly and non-invasively in a completed or annealed bilayer. Measurements of the structure of the interface can provide a basis to interpret charge transport data, guiding development towards improved performance.

The energy dependence of experimental and simulated scattering intensities of the OTFT bilayer (analogous to Fig. 4C) are shown in Fig. 5A. Again two distinct distributions are apparent. Lateral correlation lengths of 1.3 µm and 850 nm dominate the surface topography, whereas the fit correlation lengths of 35 nm and 90 nm (the result of the simple Gaussian fit to part of a lognormal distribution centered at 50 nm which can be seen in Fig. 5C) dominate the interface topography. For this sample, S_{exp} is calculated using the more prominent fits at ξ_{int} =35 nm and ξ_{surf} =1.3 µm and is shown along with the calculated sensitivity in Fig. 5B. The higher

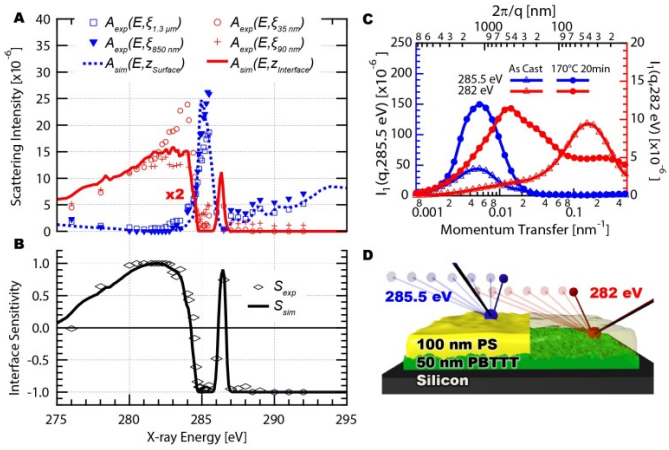

Figure 5 Organic field effect transistor results. A) Experimental and simulated scattering intensities for the OTFT sample. B) experimental and simulated interface sensitivities for the OTFT sample. C) Raw scattering intensities at the index-matched energies for the surface and interface before and after annealing. D) A schematic of the system illustrating the surface sensitivity at 285.5 eV nm and interface sensitivity at 282 eV.

degree of agreement between measured and simulated sensitivity and lower noise compared to Fig. 4D is due to optimized acquisition procedures leading to improved intensity normalization.

Because there are clear energies with high selectivity for the surface (at 285.5 eV, S <-98%) or interface (at 282 eV, S > 98%), we select E_{surf} = 285.5 eV and E_{int} = 282 eV to reveal the detailed statistical topography of the surface and interface, respectively, by examining the spatial frequency distributions .. and $I_1(q, E_{int})$. We note that the spatial frequency distribution measured here is equivalent the power spectral density of an imaging method, and thus corresponds to the analysis used in traditional roughness measurements. Fig. 5C shows these distributions for the unannealed and annealed bilayer. The RMS roughness (proportional to the integrated I_1) of the top surface increases as the in-plane spatial frequency distribution stays largely unchanged. In contrast to this, $I_1(q, E_{int})$ exhibits a complex redistribution of characteristic length scales upon annealing, on average increasing in size.

IV. METHODS

PMMA/PEG Bilayer Preparation. We produce an internal polymer-polymer interface by molding the lower layer, and setting its structure, then spin coating an upper layer of PMMA thick enough that the surface is relatively smooth. A suitable mold for the lower layer was found to be a thermally evaporated layer of Calcium Fluoride (CaF_2) approximately 200 µm thick,[33] which has an RMS

roughness of 5 nm and a characteristic shape including a dominant lateral feature size of 37 nm, illustrated in Fig 3B and measured by Atomic Force Microscopy. A mixture of poly(etheylene glycol) diacrylate 84%, Trimethylopropane Epoxylate triaxcelate 15%, and a UV sensitive crosslinker 1% was drop cast on the thermally deposited calcium fluoride and exposed to a UV lamp for ~10 seconds producing a flexible ~1 mm thick solid film. This film was released from the substrate and the CaF_2 was dissolved by water bath.

The resulting film was vacuum dried for 24 hours after which a ~400 nm thick PMMA film was deposited by spin coating in Tetrahydrofuran. The resulting bilayer was heated at 180°C (above the melting temperature of PMMA) for 24 hours, to smooth out any conformal type roughness at the top PMMA surface. The resulting surface roughness of bare substrate (with no PMMA spun on top), was measured with AFM to be ~5 nm RMS in height and ~35 nm in width, while the surface of the bilayer had a lower RMS height roughness (<1 nm) and a much larger lateral correlation length of ~1 μm (Fig S1).

PS/PBTTT Bilayer Preparation. The OTFT samples are produced on substrates of ~500 μm thick n-doped CZ Silicon (100) single side polished with 1-2 nm native oxide. Each substrate is cleaved to a 1.5 x 1.5 cm size and cleaned via standard protocols. Polystyrene (PS) M_w = 400,000, was purchased from Sigma Aldrich, GPC standard classification. Poly[2,5-bis(3-tetradecylthiophen-2-yl)thieno[3,2-b]thiophene] (PBTTT), was synthesized and donated by Dr. Martin Heeney of Imperial College and John Cowart, UCSB, under the supervision of Dr. M. Heeney. PBTTT which was used had an M_n of ~16,000. All solvents were purchased from Sigma Aldrich and are the anhydrous versions, > 98% pure. PBTTT was dissolved at 8 mg/mL in a cosolvent mixture of chlorobenzene and orthodichlorobenzene at a ratio of 1:1. PS was dissolved at 20 mg/ml in toluene under a nitrogen atmosphere. Solutions were heated to 140 ºC while stirring at 1000 rpm for 60 minutes then allowed to cool to 100 ºC stirring at 300 rpm, then filtered with a 13 mm Whatman 0.2um PTFE filter utilizing either a 3 mL glass or 1 mL NormJect syringe. Solutions were left overnight under Nitrogen and kept at 90 ºC and stirring at 300 rpm. Thin films of PBTTT were spun onto clean dry substrates from solution using a glass pipette at 1000 rpm and an acceleration of 4000 rpm/sec under ambient conditions. Samples were then dried under nitrogen at 100 ºC for 10 minutes to remove residual solvent. The PBTTT layer was ~50nm thick. The PBTTT films were allowed to dry under a nitrogen atmosphere and slowly cool to room temperature. The upper layer PS films were spun directly onto the PBTTT film from a room temperature solution using a 1 mL NormJect syringe through a 13 mm Whatman 0.2um PTFE filter spinning at 2000 rpm at an acceleration of 6000 rpm/sec. This PS layer was ~100 nm thick. One of these bilayers was subsequently annealed at 170C for 20 minutes.

Data Acquisition. Vertically polarized soft X-rays with energies between 270 and 300 eV and bandwidth of ~.1 eV were scattered from the samples at a ~2.5 degree incident grazing angle at beamline 11.0.1.2 at the Advanced Light Source.[22] This angle was chosen because it ranges from well below (at low energies) to well above the critical angle of the surface and balances intensity of scattering, which favors lower scattering angles, and depth penetration, favoring higher angles. The scattered intensity was measured from the direct specular reflection to 20 degrees in the plane of the sample by tiling three exposures of the 2D CCD detector and combining the resulting scattering patterns into a one dimensional cut of roughly 1 degree around the yoneda peak (Fig. 4A). The averaging over q_z (out of plane momentum transfer) values in this cut was found to be irrelevant, as the in plane structure was the main source of scatter, meaning plots of q_{xy} (in plane momentum transfer) at different q_z values varied only by intensity, which indicates that the structure of the scattering is predominantly in-plane. This simplifies the analysis such that the correction for variation in the out of plane direction, as is common in the distorted wave born approximation, was not necessary. The variance of intensity vs. q_z component of scatter is often also interesting [21], containing vertical depth information, however this information is also accessible through the more developed method of soft X-ray reflectivity, and so is not discussed here. The unique information we present is the in-plane structure in the off-specular direction.

V. DISCUSSION AND CONCLUSIONS

Scanning probe measurements of single layer PBTTT films have previously revealed that thermal annealing above the liquid crystal transition temperature (~145°C) increases the domain size of terraced, topographical features of an exposed surface [34-36]. Our results reveal that similar behavior is occurring at the buried interface despite the apparent divergent behavior at the exposed surface of the dielectric layer. In addition, this interfacial behavior differs from the bulk domain size evolution measured previously with polarized soft X-ray scattering.[37] This underscores the necessity of the direct in-situ measurement of the device relevant interface topography presented here (Fig. 5D).

The model systems that we present here show the possibilities for analysis available depending on the particulars of the systems probed. At the simplest level, picking out the major features in the scattering patterns by simple Gaussian fitting across the absorption edge allowed us to determine the major features in the system. Through simulation of the systems, we were then able to ascribe these features to particular materials combinations and depths within the system. Finally, by calculating the sensitivity factors S, we were able to find those specific

regions of incidence X-ray energy and grazing angle, at which each sensitivity is maximized. In these energy regions then, we can proceed beyond the initial empirical fit, and look at the details of the scattering as, in the case of an interface, the statistical spatial frequency distribution of the interfacial topography. In many cases, we suspect that regions at which sensitivity is 1 may be impossible for some features (discussed below), but even in these cases, the empirical fits of ξ give the average topological feature size.

In the two examples presented in this work, the energy at which maximum sensitivity to the interface is gained, which, by necessity means minimal sensitivity to the surface, is at 286.4 eV (PMMA/PEG) and 282 eV (PS/PBTTT). These particular energies are the energies at which the real part of the index of refraction for the upper layer, PMMA and PS respectively, equals 1 matching the refractive index of the upper layer to vacuum. In this condition, refraction from the surface is necessarily minimized. As long as the upper layer at this point also has a minimal absorption (imaginary component of the refractive index) and the lower layer has an index of refraction very different than vacuum, scattering from the lower layer, particularly the interface between the two layers is maximized. This situation is actually to be commonly expected below sharp absorption peaks because of the Kramers-Kronig relations between absorption and refraction. Thus, in the particular case of a bilayer system, finding a suitable "index-matched" energy for the upper layer is likely key to revealing structure lying below.

Additionally, in the two experiments presented, the bilayer geometry simplifies analysis of the scattering data considerably. The scattering signal is summed for many q_z values and therefore the refraction of the scattered wave at interfaces is not considered because refraction affects a wave only in the normal direction to the interfaces in question. For structures with out of plane components, this simplification would likely not hold, and modeling of both in-plane and out-of –plane directions, and further effects upon the outgoing wave may be necessary to consider. Additionally, the particular systems shown have minimal bulk scattering allowing in both experiments largely binary scattering systems, with only evidence for two major sources of scatter each. Although this should not generally be true for bilayer systems, because the layer with the most potential for bulk scattering is the upper layer, and the upper layers of the samples measured (PS and PMMA) are amorphous materials, and lack bulk variations on the mesoscopic length scales measured, it is not surprising that bulk scattering was found to not significantly contribute to scattering collected. In the case of the semicrystalline PBTTT however, the lack of bulk scattering is attributed to the highly in-plane liquid crystalline ordering. Using vertically polarized light in the grazing geometry, all orientations of in-plane oriented PBTTT have the same index of refraction. Thus, the polarized soft X-ray scatter previously observed,[37] which measured the in-plane bulk ordering behavior is avoided. In the two systems we present, we find a largely bimodal distribution of scattering peaks, which we are able to identify clearly as the top surface and internal interface, with little evidence of a scattering component corresponding to the energetic and angular dependence expected from a bulk feature. Similarly, we find no evidence of scattering from the substrate interface, which we would not expect to find in the range of topographic features probed.

In the case of conformal roughness, GRSoXS may be of great use however the formalism developed here of independent surface morphologies would not be appropriate, as if the morphologies would be the same the scattering pattern when illuminating the surface and the internal interface would be the same. The identification of conformal roughness would be trivial. By going to an index-matched energy for the upper layer, at which point scattering from the vacuum interface should be minimized, observation of the same pattern seen at an energy at which *only* the surface can be contributing (e.g. below the critical angle, or at absorption peaks where penetration depths are only a few nm) is strong evidence of conformal roughness.

In the case of films with very rough surfaces, where the local incident angle of the X-rays varies widely, and shadowing is a possibility (effectively negative local incident angles) an altered version of the XEFI derivation would need to be employed.[27] The incident angle becomes less and less important as the local slope distribution of the top interface of the film widens. This smears out the XEFI vs incident angle lowering the complexity of the parameter space (Fig. 3A), with both the benefits (easier to explore) and detriments (harder to find a location with high interfacial sensitivity) to an experiment.

To apply this technique to inorganic systems, it will be critical to pick an absorption edge that allows the scatter and refraction from the upper layer to be varied significantly, in order to observe the potentially small signal of the structure of interest from within the film. As a benefit, at other edges, the limiting wavelength may be considerably different (ie 2 nm for oxygen Kα or 0.5 nm for Sulfur Kα), allowing smaller scale features to be resolved. In some cases, an index-matched condition may be impossible, because the material might not contain a dominant enough element with a suitably sharp absorption edge. However, in the measured indices of refraction for common polymers previously published,[38] this behavior occurs in essentially all cases. For other edges, previous studies have, for example, shown that Gd at the $Gd_{4,5}$ edge (~1200 eV)[39] and $YBa_2Cu_3O_{6+\delta}$ at the copper L_3 edge (~930 eV),[40] both have suitable regions where δ crosses zero and β is low. Hence, suitable energies where δ crosses zero are likely for the all the transition metals with edges in the 280 to 1200 eV range, as well as for oxides and nitrides at the oxygen and nitrogen absorption edges.

We have demonstrated the use of GRSoXS to determine in-plane spatial frequency distributions of buried polymer-polymer interfaces and measured the interface topography and its evolution upon processing in an OTFT bilayer. In addition, we have presented a simple model to predict scattering intensities, which allows unambiguous identification of scatter at different energies to specific internal film features. Future experiments with current experimental parameters can potentially reveal dynamics of interface reorganization by measuring I_1 with 5 s temporal resolution. The range of length scales presently probed by GRSoXS is also highlighted by Fig. 5C, with sensitivity spanning three orders of magnitude, limited by wavelength (4 nm) and coherence of the beamline (5 μm)[22] readily achievable.

Detailed structure-function relations can now be established for a wide range of thin film systems for which the buried structure critically determines function. The present work clearly illustrates the applicability to organic bilayer systems such as OTFTs and organic light emitting diodes. [41] A clear extension of the method is to examine systems with non-planar interfaces, measuring the complex structure as a function of depth that occur, for example, in bulk heterojunction excitonic solar cells.[42, 43] In addition, numerous inorganic systems including oxide heterostructures[44] contain buried functional interfaces where differences in optical properties at other absorption edges can be exploited. We envision GRSoXS as an extremely versatile tool for establishing structure-function correlations at these and many other device-relevant interfaces.

ACKNOWLEDGEMENTS

Data was acquired at beamline 11.0.1.2 of the Advanced Light Source in Berkeley [22] and available by contacting ehgann@ncsu.edu. Analysis and Modeling code is available by contacting ehgann@ncsu.edu. The Advanced Light Source is supported by the Director, Office of Science, Office of Basic Energy Sciences, of the U.S. Department of Energy under Contract No. DE-AC02-05CH11231. Discussions and insights from D.B. Dougherty, A. Hexemer, J. Kortright, and A. Young are acknowledged. Research at NCSU was supported by NSF (DMR-0906457 and 1207032), UCSB by NSF (DMR 0906224). E. Gann was partially supported by a GAANN Fellowship.

1 H. Lüth, *Solid surfaces, interfaces and thin films* (Springer, Heidelberg ; New York, 2010).
2 R. J. Kline, M. D. McGehee, and M. F. Toney, Nat. Mater. **5**, 222 (2006).
3 S. J. Haigh, et al., Nat. Mater. **11**, 764 (2012).
4 T. R. Albrecht, P. Grutter, D. Horne, and D. Rugar, J. Appl. Phys. **69**, 668 (1991).
5 D. A. Chen, A. Nakahara, D. G. Wei, D. Nordlund, and T. P. Russell, Nano Lett. **11**, 561 (2011).
6 J. W. Kiel, B. J. Kirby, C. F. Majkrzak, B. B. Maranville, and M. E. Mackay, Soft Matter **6**, 641 (2010).
7 H. Yan, et al., J. Appl. Phys. **110**, 102220 (2011).
8 P. Gupta, A. K. Sinha, M. H. Modi, S. M. Gupta, P. K. Gupta, and S. K. Deb, Appl. Surf. Sci. **257**, 210 (2010).
9 R. J. Roe, *Methods of X-Ray and Neutron Scattering in Polymer Science* (Oxford University Press, New York, 2000).
10 P. Muller-Buschbaum, J. S. Gutmann, and M. Stamm, Phys. Chem. Chem. Phys. **1**, 3857 (1999).
11 S. K. Sinha, J. Phys. III **4**, 1543 (1994).
12 G. Renaud, R. Lazzari, and F. Leroy, Surf. Sci. Rep. **64**, 255 (2009).
13 G. Renaud, et al., Science **300**, 1416 (2003).
14 Z. Jiang, D. R. Lee, S. Narayanan, J. Wang, and S. K. Sinha, Phys. Rev. B **84**, 075440 (2011).
15 O. Glatter and O. Kratky, *Small Angle X-Ray Scattering* (Academic Press, New York, 1982).
16 N. Stribeck, *X-Ray Scattering of Soft Matter* (Springer, Berlin, Berlin, 2007).
17 J. P. Simon, O. Lyon, and D. Defontaine, J. Appl. Crystallogr. **18**, 230 (1985).
18 T. Araki, H. Ade, J. M. Stubbs, D. C. Sundberg, G. Mitchell, J. B. Kortright, and A. L. D. Kilcoyne, Appl. Phys. Lett. **89**, 124106 (2006).
19 G. E. Mitchell, B. G. Landes, J. Lyons, B. J. Kern, M. J. Devon, I. Koprinarov, E. M. Gullikson, and J. B. Kortright, Appl. Phys. Lett. **89**, 044101 (2006).
20 P. Andreazza, H. Khelfane, O. Lyon, C. Andreazza-Vignolle, A. Y. Ramos, and M. Samah, Eur. Phys. J. Spec. Top. **208**, 231 (2012).
21 M. A. Ruderer, C. Wang, E. Schaible, A. Hexemer, T. Xu, and P. Müller-Buschbaum, Macromolecules **46**, 4491 (2013).
22 E. Gann, A. T. Young, B. A. Collins, H. Yan, J. Nasiatka, H. A. Padmore, H. Ade, A. Hexemer, and C. Wang, Rev. Sci. Instrum. **83**, 045110 (2012).
23 Y. Murakami, et al., Phys. Rev. Lett. **81**, 582 (1998).
24 S. Smadici, J. C. T. Lee, S. Wang, P. Abbamonte, G. Logvenov, A. Gozar, C. D. Cavellin, and I. Bozovic, Phys. Rev. Lett. **102**, 107004 (2009).
25 B. Watts, S. Swaraj, D. Nordlund, J. Luning, and H. Ade, J. Chem. Phys. **134**, 024702 (2011).
26 H. Ade and A. P. Hitchcock, Polymer **49**, 643 (2008).

[27] M. Tolan, *X-ray scattering from soft-matter thin films : materials science and basic research* (Springer, Berlin ; New York, 1999).
[28] See Supplemental Material at [URL will be inserted by publisher] for detailed two dimensional cuts of the XEFI.
[29] See Supplemental Material at [URL will be inserted by publisher] for discussion of uncertainty.
[30] See Supplemental Material at [URL will be inserted by publisher] for the full dataset.
[31] H. Yan, T. Schuettfort, A. J. Kronemeijer, C. R. McNeill, and H. W. Ade, Appl. Phys. Lett. **101**, 093308 (2012).
[32] H. Sirringhaus, Adv. Mater. **17**, 2411 (2005).
[33] T. Kerle, Z. Q. Lin, H. C. Kim, and T. P. Russell, Macromolecules **34**, 3484 (2001).
[34] I. Mcculloch, et al., Nat. Mater. **5**, 328 (2006).
[35] D. M. DeLongchamp, R. J. Kline, D. A. Fischer, L. J. Richter, and M. F. Toney, Adv. Mater. **23**, 319 (2011).
[36] T. Schuettfort, B. Watts, L. Thomsen, M. Lee, H. Sirringhaus, and C. R. McNeill, ACS Nano **6**, 1849 (2012).
[37] B. A. Collins, et al., Nat. Mater. **11**, 536 (2012).
[38] B. Watts, S. Swaraj, D. Nordlund, J. Lüning, and H. Ade, J. Chem. Phys. **134**, 024702 (2011).
[39] J. F. Peters, J. Miguel, M. A. de Vries, O. M. Toulemonde, J. B. Goedkoop, S. S. Dhesi, and N. B. Brookes, Phys. Rev. B **70**, 224417 (2004).
[40] D. G. Hawthorn, et al., Phys. Rev. B **84**, 075125 (2011).
[41] M. T. Bernius, M. Inbasekaran, J. O'Brien, and W. S. Wu, Adv. Mater. **12**, 1737 (2000).
[42] G. Li, R. Zhu, and Y. Yang, Nature Photon. **6**, 153 (2012).
[43] G. Yu, J. Gao, J. C. Hummelen, F. Wudl, and A. J. Heeger, Science **270**, 1789 (1995).
[44] M. Salluzzo, et al., Adv. Mater. **25**, 2333 (2013).